Journal of Power Sources 193 (2009) 93–98

Contents lists available at ScienceDirect

Journal of Power Sources

journal homepage: www.elsevier.com/locate/jpowsour

Effect of oxygen vacancies on electrical properties of $Ce_{0.8}Sm_{0.1}Nd_{0.1}O_{2-\delta}$ electrolyte: An in situ Raman spectroscopic study

Shi-Ping Li, Ji-Qing Lu, Ping Fang, Meng-Fei Luo*

Zhejiang Key Laboratory for Reactive Chemistry on Solid Surfaces, Institute of Physical Chemistry, Zhejiang Normal University, Jinhua 321004, PR China

ARTICLE INFO

Article history:
Received 5 September 2008
Received in revised form 4 December 2008
Accepted 4 December 2008
Available online 11 December 2008

Keywords:
Solid oxide fuel cells
Conductivity
Oxygen vacancies
Grain size
In situ Raman spectroscopy

ABSTRACT

$Ce_{0.8}Sm_{0.2}O_{2-\delta}$, $Ce_{0.8}Nd_{0.2}O_{2-\delta}$ and $Ce_{0.8}Sm_{0.1}Nd_{0.1}O_{2-\delta}$ samples were prepared by a citrate sol–gel method. Effects of microstructures and oxygen vacancies of the samples on their electrical properties were investigated by X-ray diffraction (XRD), scanning electron microscope (SEM), in situ Raman spectroscopy and AC impedance spectroscopy. SEM results indicated that larger grains were formed on the $Ce_{0.8}Nd_{0.2}O_{2-\delta}$ and $Ce_{0.8}Sm_{0.1}Nd_{0.1}O_{2-\delta}$ electrolytes compared to that on the $Ce_{0.8}Sm_{0.2}O_{2-\delta}$. In situ Raman spectra suggested that the concentration of oxygen vacancies of the $Ce_{0.8}Sm_{0.1}Nd_{0.1}O_{2-\delta}$ sample was the highest while that of $Ce_{0.8}Sm_{0.2}O_{2-\delta}$ was the lowest. It was found that the difference in the electrical conductivity for these electrolytes was closely related to the microstructure and oxygen vacancies of the samples. The highest electrical conductivity obtained on the $Ce_{0.8}Sm_{0.1}Nd_{0.1}O_{2-\delta}$ sample was ascribed to its larger grain size and higher concentration of oxygen vacancies.

1. Introduction

Rare earth doped-ceria solid electrolytes are of growing interest for their applications in intermediate temperature (600–700 °C) solid oxide fuel cells (IT-SOFCs), due to their higher electrical conductivities compared to the traditional yttria stabilized zirconia (YSZ) [1,2]. Since the single-doped-ceria may inevitably result in excessive electronic conductivity and low energy conversion efficiency under low oxygen partial pressure around the temperature of 700 °C [3], structural modification of ceria solid electrolyte is desirable. It has been reported that co-doping with cations such as Pr [4], La [5], Y [6], and Ca [7] into $Ce_{0.8}Sm_{0.2}O_{2-\delta}$ system is effective to improve the ionic conductivity and reduce the electronic conductivity of $Ce_{0.8}Sm_{0.2}O_{2-\delta}$ at lower temperature.

In doped-ceria system, after partial substitution of Ce^{4+} with trivalent rare earth or divalent alkaline-earth cations the oxygen vacancies increase significantly, which could consequently enhance the electrical conductivity. Raman spectroscopy is a powerful technique which could be used to study the oxygen vacancies in the CeO_2-based solid solution [8]. For example, Peng et al. [9] studied a $Ce_{1-x}Sm_xO_{2-\delta}$ system using Raman spectroscopy and concluded that a high electrical conductivity was contributed to a higher concentration of oxygen vacancies in the sample.

As mentioned above, Raman spectroscopy could be used to study the influence of oxygen vacancies on electrical conductivity of the CeO_2-based solid solution. However, these investigations were usually carried out at room temperature. Since electrical conductivity was always studied above 300 °C, it is desirable to run the investigation at working temperature, in order to provide relevant information of the relationship between oxygen vacancies and electrical conductivity. Therefore, in this paper, in situ Raman spectroscopy was used to study the effect of oxygen vacancies on electrical conductivity of a co-doped solid solution of CeO_2–Sm_2O_3–Nd_2O_3 system. Besides, the influence of morphologies of the electrolytes on electrical conductivity was also investigated.

2. Experimental

2.1. Sample preparation

$Ce_{0.8}Sm_{0.2}O_{2-\delta}$, $Ce_{0.8}Nd_{0.2}O_{2-\delta}$ and $Ce_{0.8}Sm_{0.1}Nd_{0.1}O_{2-\delta}$ samples were prepared by a citrate sol–gel method [10], using $Ce(NO_3)_3{\cdot}6H_2O$, Sm_2O_3 and Nd_2O_3 as the starting materials. For the preparation of the $Ce_{0.8}Sm_{0.1}Nd_{0.1}O_{2-\delta}$ sample, an aqueous solution of cerium nitrate was mixed with stoichiometric amounts of Sm_2O_3 and Nd_2O_3 dissolved in the least amount of concentrated nitrate acid. Then citric acid with double molar amount of the metal ions (Ce + Sm + Nd) was added into the above solution. The as-prepared pellucid solution was heated at 80 °C on a water-bath and continuously stirred for several hours until a viscous gel was obtained. The gel was dried at 120 °C overnight and then calcined at 600 °C for 4 h in air. The resulting sample was denoted as A600. Thoroughly, the calcined sample (A600) was substantially ground in an agate

* Corresponding author. Fax: +86 579 82282595.
E-mail address: mengfeiluo@zjnu.cn (M.-F. Luo).

0378-7753/$ – see front matter.
doi:10.1016/j.jpowsour.2008.12.022

mortar and then pressed into cylindrical pellets at a pressure of 400 MPa. The pellets were sintered at 1500 °C for 4 h in air with a heating rate of 3 °C min^{-1} and the resulting sample was denoted as A1500. Other samples were prepared in a similar manner.

2.2. Characterizations

X-ray diffraction (XRD) patterns of the powder samples were collected on a Philips PW 3040/60 powder diffractometer using Cu Kα radiation (λ = 0.1542 nm). The working voltage was 40 kV and the working current was 40 mA. The intensity data were collected at room temperature with a scanning range of 20–90°. The average crystallite sizes and the lattice parameters of the samples were calculated by a full curve fitting method using JADE 6.5 software.

Surface morphologies of the sintered pellets (A1500) were analyzed in a Hitachi S-4800 scanning electron microscope (SEM).

Raman spectra of the sintered samples (A1500) were obtained with a Renishaw RM1000 with a confocal microprobe. A 514 nm excitation laser line, a dwell time of 2 s, twice scans, and a resolution of 1 cm^{-1} were used for the Raman experiments. A power of 10% for the 514 nm excitation laser line (Ar^+ laser) was used. In situ Raman measurements of the samples were performed in a homemade in situ Raman cell linked to the Raman equipment. About 20 mg of the powder sample was inserted into the cell and heated up to 500 °C under O_2 for 1 h with a heating rate of 20 °C min^{-1}, then it was cooled down to room temperature and exposed to air atmosphere. The sample was again heated up from room temperature to 600 °C at a heating rate of 10 °C min^{-1} for spectra collection. Prior to the spectra collection, each temperature point was held for 10 min.

Electrical conductivities of the samples were measured on the sintered pellets (A1500). Both faces of the pellets were polished using emery papers, and Pt electrodes prepared by painting with Pt paste and fired at 1000 °C for half hour were deposited on the smooth faces. The AC impedance spectra of the sintered samples were obtained in air atmosphere with a Princeton Applied Research (PAR) Model 283 potentiostat and the model 1025 frequency response detector. The samples were heated during the measurement in a homemade furnace. The test frequencies range from 0.1 Hz to 4 MHz and the measurements were conducted at a temperature range of 300–600 °C with an interval of 100 °C. A Ziew 2.0 software was used to analyze the impedance data and calculate the electrical conductivity of the samples.

3. Results and discussion

3.1. XRD patterns

Fig. 1 shows the XRD patterns of the CeO_2, $Ce_{0.8}Sm_{0.2}O_{2-\delta}$, $Ce_{0.8}Nd_{0.2}O_{2-\delta}$ and $Ce_{0.8}Sm_{0.1}Nd_{0.1}O_{2-\delta}$ samples calcined 600 °C and sintered at 1500 °C. All the samples only show diffraction peaks due to cubic fluoride phase of CeO_2 even after high-temperature sintering. Compared to the pure CeO_2, the patterns of the $Ce_{0.8}Sm_{0.2}O_{2-\delta}$, $Ce_{0.8}Nd_{0.2}O_{2-\delta}$ and $Ce_{0.8}Sm_{0.1}Nd_{0.1}O_{2-\delta}$ samples shift slightly to lower angle. Moreover, no noticeable diffraction peaks due to Ce_2O_3 is observed, which has a feature peak at 2 theta of 26.73° [11].

Lattice parameters and crystallite sizes of the CeO_2, $Ce_{0.8}Sm_{0.2}O_{2-\delta}$, $Ce_{0.8}Nd_{0.2}O_{2-\delta}$ and $Ce_{0.8}Sm_{0.1}Nd_{0.1}O_{2-\delta}$ samples analyzed by JADE 6.5 software are listed in Table 1. The lattice parameters for the doped-ceria samples are larger than that of the pure CeO_2. It could be attributed to the incorporation of the larger cations of Sm^{3+} (0.1219 nm) or Nd^{3+} (0.1249 nm) into the CeO_2 lattice, which causes lattice expansion [12]. These findings indicate the formation of CeO_2-based solid solution. The crystallite sizes of the A600 samples are within nano-scale with an average crystal size of 11–28 nm. Note that the crystallite sizes of the doped-ceria are smaller than that of the pure ceria, because the addition of other cations into CeO_2 leads to retardation of crystallite growth due to the solute drag effect [13]. For the sintered samples (A1500), the crystallites are so large that they beyond the analysis range of the JADE 6.5 software and therefore the results are not listed.

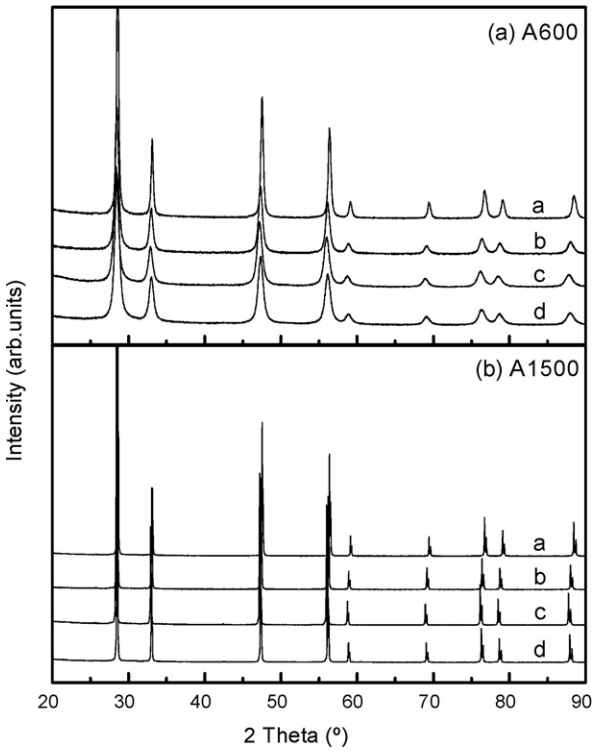

Fig. 1. XRD patterns of (a) CeO_2; (b) $Ce_{0.8}Sm_{0.2}O_{2-\delta}$; (c) $Ce_{0.8}Nd_{0.2}O_{2-\delta}$; and (d) $Ce_{0.8}Sm_{0.1}Nd_{0.1}O_{2-\delta}$ samples (a) calcined at 600 °C (A600) and (b) sintered at 1500 °C (A1500).

3.2. SEM

The microstructures of the $Ce_{0.8}Sm_{0.2}O_{2-\delta}$, $Ce_{0.8}Nd_{0.2}O_{2-\delta}$ and $Ce_{0.8}Sm_{0.1}Nd_{0.1}O_{2-\delta}$ samples sintered at 1500 °C are shown in Fig. 2. No crack is detected. The average grain sizes of the $Ce_{0.8}Sm_{0.2}O_{2-\delta}$, $Ce_{0.8}Nd_{0.2}O_{2-\delta}$ and $Ce_{0.8}Sm_{0.1}Nd_{0.1}O_{2-\delta}$ are approximately 0.3–0.7 μm. Furthermore, it is obvious that the grain sizes of the $Ce_{0.8}Nd_{0.2}O_{2-\delta}$ and $Ce_{0.8}Sm_{0.1}Nd_{0.1}O_{2-\delta}$ are larger than that of the $Ce_{0.8}Sm_{0.2}O_{2-\delta}$.

3.3. Raman spectra

Fig. 3 shows the in situ Raman spectra of the $Ce_{0.8}Sm_{0.2}O_{2-\delta}$, $Ce_{0.8}Nd_{0.2}O_{2-\delta}$ and $Ce_{0.8}Sm_{0.1}Nd_{0.1}O_{2-\delta}$ samples sintered at

Table 1
Lattice parameters and crystallite sizes of CeO_2, $Ce_{0.8}Sm_{0.2}O_{2-\delta}$, $Ce_{0.8}Nd_{0.2}O_{2-\delta}$ and $Ce_{0.8}Sm_{0.1}Nd_{0.1}O_{2-\delta}$ samples calcined at 600 °C (A600) and sintered at 1500 °C (A1500).

Sample	A600		A1500
	Lattice parameter (nm)	Crystallite size (nm)	Lattice parameter (nm)
CeO_2	0.5411 (3)	28	0.5414 (4)
$Ce_{0.8}Sm_{0.2}O_{2-\delta}$	0.5435 (3)	15	0.5437 (1)
$Ce_{0.8}Nd_{0.2}O_{2-\delta}$	0.5446 (1)	12	0.5447 (1)
$Ce_{0.8}Sm_{0.1}Nd_{0.1}O_{2-\delta}$	0.5440 (2)	11	0.5442 (3)

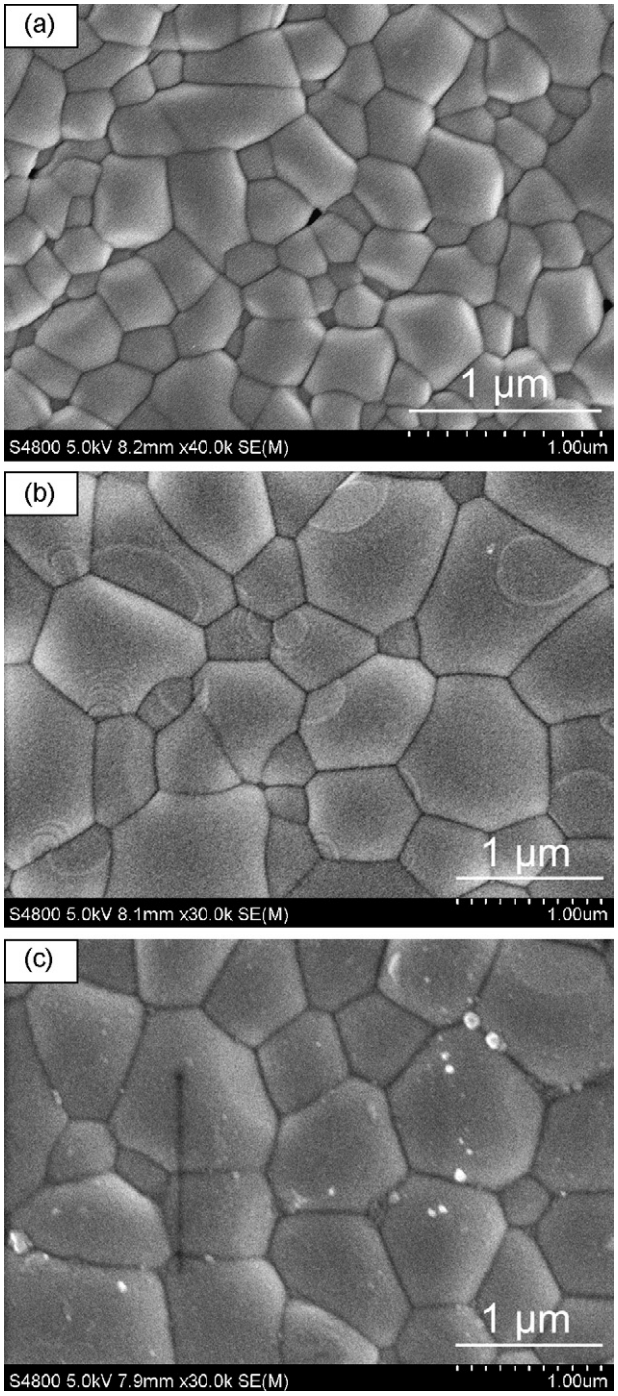

Fig. 2. SEM images of (a) $Ce_{0.8}Sm_{0.2}O_{2-\delta}$; (b) $Ce_{0.8}Nd_{0.2}O_{2-\delta}$; and (c) $Ce_{0.8}Sm_{0.1}Nd_{0.1}O_{2-\delta}$ electrolytes.

1500 °C, which are measured at temperature range of 300–600 °C. It can be seen that each Raman spectrum consists of two distinctive peaks. One intensive peak at 460 cm^{-1} is attributed to the F_{2g} vibration mode of the fluorite structure of pure CeO_2, and the other weak peak at 570 cm^{-1} is ascribed to oxygen vacancies [8].

According to our previous work [14], the concentration of oxygen vacancies was determined by the ratio of the peak areas of the bands at 460 (A_{460}) and 570 cm^{-1} (A_{570}) based on the spectra in Fig. 3. The A_{570}/A_{460} ratio reflects the concentration of oxygen vacancies in the CeO_2-based solid solution. The relationship between A_{570}/A_{460} and temperature is shown in Fig. 4. It is found that the values of A_{570}/A_{460}

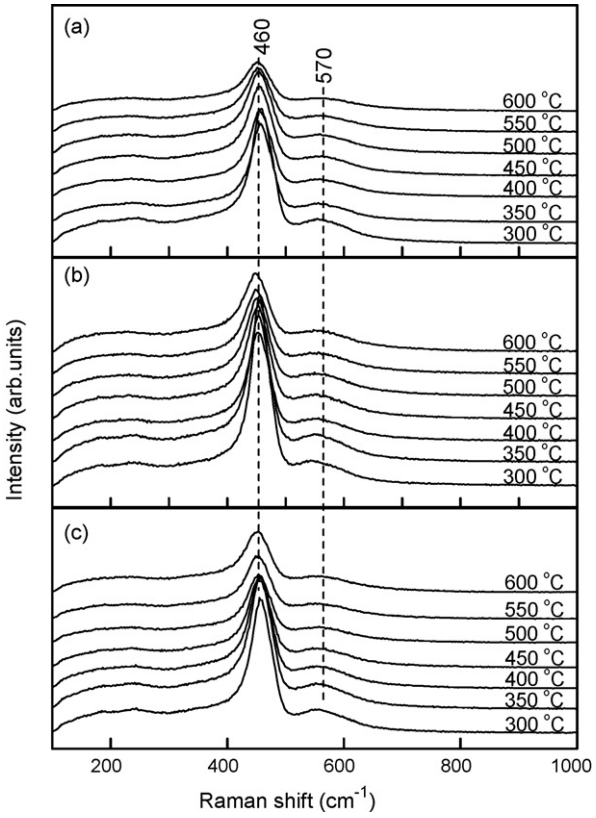

Fig. 3. In situ Raman spectra of (a) $Ce_{0.8}Sm_{0.2}O_{2-\delta}$; (b) $Ce_{0.8}Nd_{0.2}O_{2-\delta}$: and (c) $Ce_{0.8}Sm_{0.1}Nd_{0.1}O_{2-\delta}$ samples sintered at 1500 °C and measured at temperature range of 300–600 °C.

for all the samples increase with increasing temperature. This could be explained as follows: $V_o^{\bullet\bullet}$ (oxygen vacancy) is formed when Sm_2O_3 is doped into CeO_2 lattice in order to maintain the electrical neutrality. At lower temperature, Sm'_{Ce} (Sm^{3+} on a Ce^{4+} lattice site) and $V_o^{\bullet\bullet}$ form defect associates $\{Sm'_{Ce}, V_o^{\bullet\bullet}\}$ under coulomb forces interaction. As the measuring temperature increases, the $\{Sm'_{Ce}, V_o^{\bullet\bullet}\}$ pairs gradually dissociate to free oxygen vacancy ($V_o^{\bullet\bullet}$) [15] and consequently increases the amount of oxygen vacancies. In addition, the A_{570}/A_{460} value for the $Ce_{0.8}Sm_{0.1}Nd_{0.1}O_{2-\delta}$ sample is the highest and the $Ce_{0.8}Nd_{0.2}O_{2-\delta}$ sample is appreciably higher than that of the $Ce_{0.8}Sm_{0.2}O_{2-\delta}$, due to different configuration of oxygen vacancies and dopants for the three samples [16].

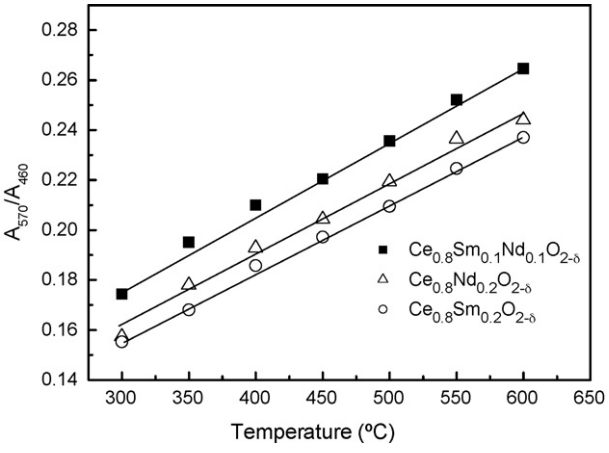

Fig. 4. Relationship between A_{570}/A_{460} and temperature for CeO_2-based samples.

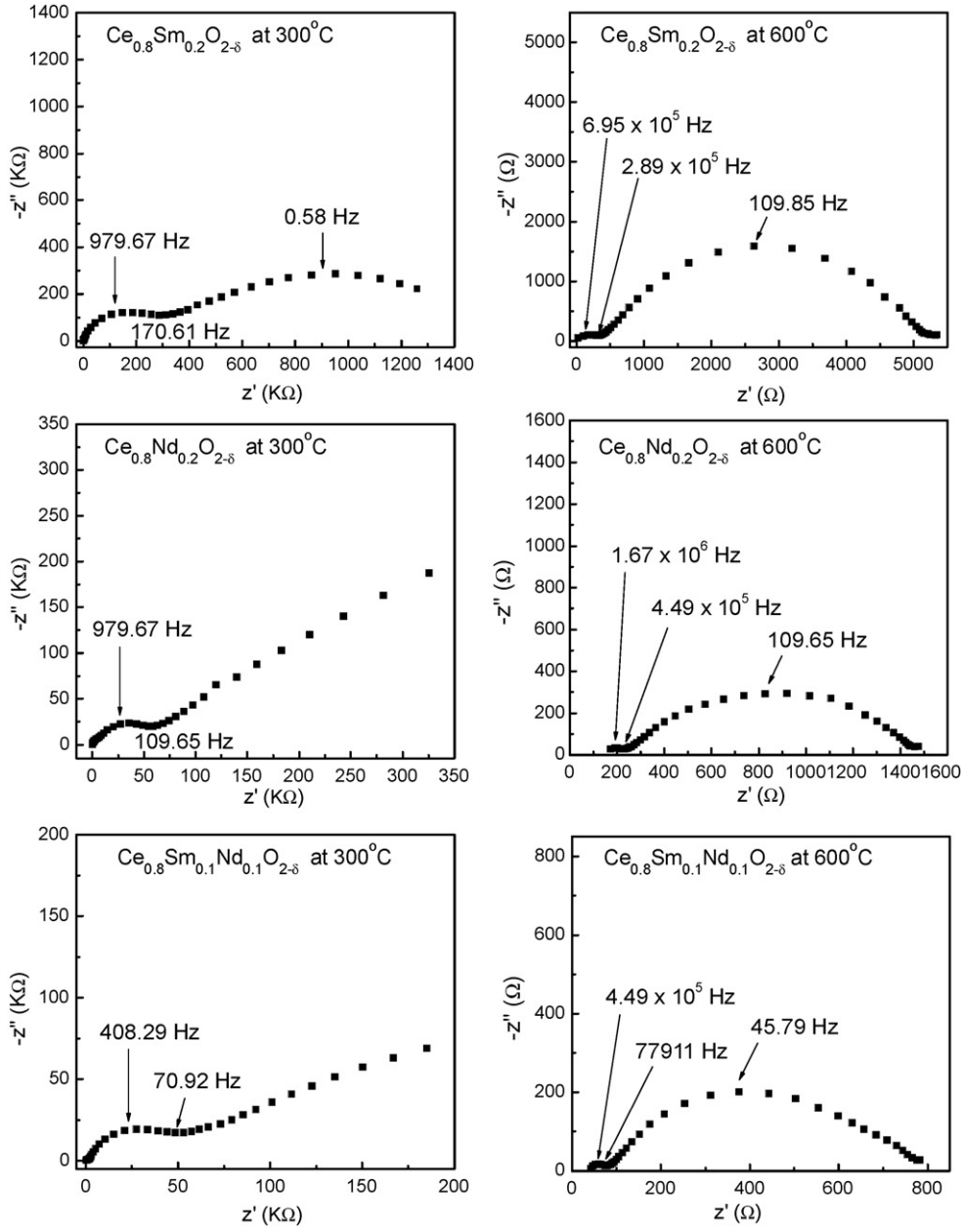

Fig. 5. Impedance spectra of $Ce_{0.8}Sm_{0.2}O_{2-\delta}$, $Ce_{0.8}Nd_{0.2}O_{2-\delta}$ and $Ce_{0.8}Sm_{0.1}Nd_{0.1}O_{2-\delta}$ electrolytes at 300 and 600 °C.

3.4. Electrical properties

The AC impedance spectra of the $Ce_{0.8}Sm_{0.2}O_{2-\delta}$, $Ce_{0.8}Nd_{0.2}O_{2-\delta}$ and $Ce_{0.8}Sm_{0.1}Nd_{0.1}O_{2-\delta}$ measured at 300 and 600 °C are presented in Fig. 5. The AC impedance is a well-suited technique for separating out grain interior, grain boundary and electrode polarization contributions to the total electrical conductivity of the sintered samples. Generally, the idealized impedance spectra consist of three semicircles. The semicircles represent grain interior, grain boundary and electrode polarization resistances at high, intermediate and low frequency, respectively [17].

It is clear that all the spectra in Fig. 5 show a depressed semicircle and a spike originated at low temperature (300 °C). As the measuring temperature increases, the depressed semicircle associated with the resistances of grain interior and grain boundary becomes smaller. Meanwhile, the spike corresponding to electrode polarization process turns to a semicircle. The impedance spectra can be modeled with the equivalent circuit shown in Fig. 6. R_0 represents the unavoidable resistance associated with testing equipment design. Rgi is the grain interior resistance in parallel with the capcitor (Cgi). CPEgb, CPEct, Rgb and Rct are the grain boundary, electrode polarization constant phase element, grain boundary and electrode polarization resistance, respectively.

For analysis of the total resistance, the grain interior and grain boundary resistances are combined. The electrical conductivity data are calculated and plotted in Fig. 7. It can be seen that the electrical conductivities exhibit the Arrhenius behavior. Meanwhile,

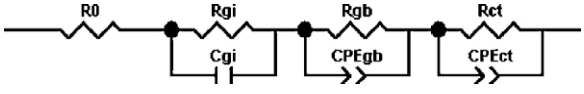

Fig. 6. Equivalent circuit used in analyzing impedance spectra.

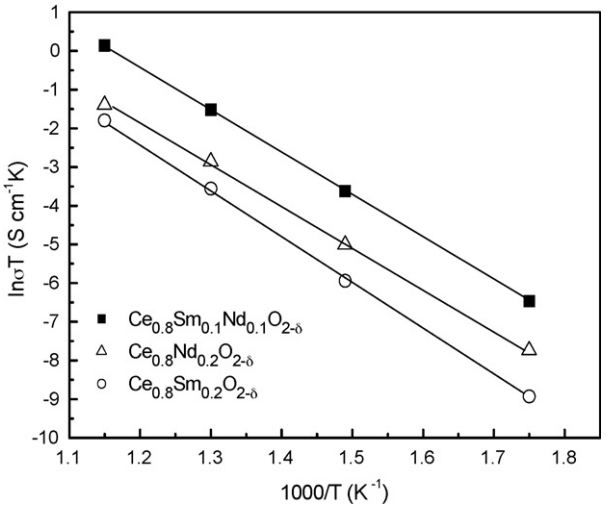

Fig. 7. Temperature dependence of total electrical conductivity of $Ce_{0.8}Sm_{0.2}O_{2-\delta}$, $Ce_{0.8}Nd_{0.2}O_{2-\delta}$ and $Ce_{0.8}Sm_{0.1}Nd_{0.1}O_{2-\delta}$ electrolytes.

these data obey the Arrhenius equation:

$$\sigma = \frac{\sigma_0}{T} \exp\left(\frac{-E_a}{kT}\right) \quad (1)$$

where E_a is the activation energy of electrical conduction; k is the Boltzmann constant; T is the temperature in Kelvin; and σ_0 is a constant of pre-exponential factor. The activation energies for all the samples are calculated and listed in Table 2.

As shown in Table 2, it can be seen that for the different doped materials, the conductivities vary substantially, while there is no significant difference in the activation energy. Meanwhile, the electrical conductivity of $Ce_{0.8}Sm_{0.1}Nd_{0.1}O_{2-\delta}$ is 132.30×10^{-5} S cm^{-1}, which is obviously higher than that of the $Ce_{0.8}Nd_{0.2}O_{2-\delta}$ (28.40×10^{-5} S cm^{-1}) and the $Ce_{0.8}Sm_{0.2}O_{2-\delta}$ (20.00×10^{-5} S cm^{-1}) at 600 °C. This could be explained by the different microstructures of the samples. As shown in Fig. 2, dense solid electrolytes are prepared, thus the effect of pores could be ignored and electrical conductivities of the electrolytes are mainly made up of grain interior and grain boundary conductivity. As is known, the conductivity of grain boundary is affected by the intergranular regions and the conductivity of grain boundary is 2–3 times less than that of the grain interior [18,19]. Therefore, reducing grain boundary namely the intergranular region on per unit area could effectively enhance the grain boundary conductivity and further increase the total conductivity. Compared with the $Ce_{0.8}Sm_{0.2}O_{2-\delta}$, the grain sizes of $Ce_{0.8}Nd_{0.2}O_{2-\delta}$ and $Ce_{0.8}Sm_{0.1}Nd_{0.1}O_{2-\delta}$ are larger, and the grain boundary is smaller, so the electrical conductivities of these two samples could be improved.

However, the difference in the electrical conductivities of the $Ce_{0.8}Nd_{0.2}O_{2-\delta}$ and $Ce_{0.8}Sm_{0.1}Nd_{0.1}O_{2-\delta}$ electrolytes could not be simply explained by the microstructure deviation, as the SEM results show that these two samples have similar grain sizes and grain boundary. Therefore, the difference may lie in the different chemical natures of these two samples, which is discussed below.

Previous study pointed out that the enhanced electrical conductivity of co-doped-ceria samples with respect to single-doped-ceria was contributed to the increase of oxygen vacancy concentrations [20]. In the present study, the in situ Raman spectroscopy results clearly show that for each individual sample, the concentration of oxygen vacancies increases with increasing temperature, which shows the same trend with the corresponding electrical conductivities. This suggests that the oxygen vacancies play an important role in the electrical conductivity of the sample, as well as the microstructure. Compared to the $Ce_{0.8}Sm_{0.2}O_{2-\delta}$ sample, the $Ce_{0.8}Nd_{0.2}O_{2-\delta}$ and $Ce_{0.8}Sm_{0.1}Nd_{0.1}O_{2-\delta}$ exhibit the higher electrical conductivities, which may be contributed to the larger grain size and much higher concentration of oxygen vacancies in these samples. Furthermore, when comparing the $Ce_{0.8}Nd_{0.2}O_{2-\delta}$ and the $Ce_{0.8}Sm_{0.1}Nd_{0.1}O_{2-\delta}$ samples, the $Ce_{0.8}Sm_{0.1}Nd_{0.1}O_{2-\delta}$ sample has a concentration of oxygen vacancies than the $Ce_{0.8}Nd_{0.2}O_{2-\delta}$ sample. Therefore, the higher conductivity of the $Ce_{0.8}Sm_{0.1}Nd_{0.1}O_{2-\delta}$ sample is due to its higher concentration of oxygen vacancies, since the grain sizes of these two samples are very similar. This result is in accordance with the previous literature, in which the authors correlated the higher conductivity to the higher concentration of oxygen vacancies in the $Ce_{1-x}Sm_xO_{2-\delta}$ system [9].

Table 2
Total conductivity (σ) and activation energy (E_a) of $Ce_{0.8}Sm_{0.2}O_{2-\delta}$, $Ce_{0.8}Nd_{0.2}O_{2-\delta}$ and $Ce_{0.8}Sm_{0.1}Nd_{0.1}O_{2-\delta}$ electrolytes.

Sample	σ ($\times 10^{-5}$ S cm^{-1})				E_a (eV)
	300 °C	400 °C	500 °C	600 °C	300–600 °C
$Ce_{0.8}Sm_{0.2}O_{2-\delta}$	0.02	0.39	3.69	20.00	1.02 ± 0.015
$Ce_{0.8}Nd_{0.2}O_{2-\delta}$	0.08	0.99	7.39	28.40	0.91 ± 0.018
$Ce_{0.8}Sm_{0.1}Nd_{0.1}O_{2-\delta}$	0.27	3.96	28.05	132.30	0.95 ± 0.003

4. Conclusions

A series of dense CeO_2-based solid solution electrolytes were prepared and their electrical conductivities were measured. It was found that the electrical conductivities of the CeO_2-base solid electrolytes depended on not only their microstructures but greatly oxygen vacancies of the samples. The $Ce_{0.8}Sm_{0.1}Nd_{0.1}O_{2-\delta}$ sample exhibited higher electrical conductivity than the $Ce_{0.8}Sm_{0.2}O_{2-\delta}$ and $Ce_{0.8}Nd_{0.2}O_{2-\delta}$ samples, due to its larger grain size and higher concentration of oxygen vacancies. Our work demonstrates that co-doping of ceria with Nd and Sm is effective to improve the electrical conductivity, and the $Ce_{0.8}Sm_{0.1}Nd_{0.1}O_{2-\delta}$ could be a promising electrolyte material for application in intermediate temperature solid oxide fuel cells.

Acknowledgments

This work was supported by the Natural Science Foundation of Zhejiang Province (Grant No. Z404383) and the National Science Foundation of China (Grant No.20873125).

References

[1] T.H. Etsell, S.N. Flengas, Chem. Rev. 70 (1970) 339–376.
[2] O. Bellon, N.M. Sammes, J. Staniforth, J. Power Sources 75 (1998) 116–121.
[3] G.B. Jung, T.J. Huang, J. Mater. Sci. 38 (2003) 2461–2468.
[4] W. Huang, P. Shuk, M. Greenblatt, Solid State Ionics 113–115 (1998) 305–310.
[5] M. Dudek, W. Bogusz, Ł. Zych, B. Trybalska, Solid State Ionics 179 (2008) 164–167.
[6] X.Q. Sha, Z. Lü, X.Q. Huang, J.P. Miao, Z.G. Liu, X.S. Xin, Y.H. Zhang, W.H. Su, J. Alloys Compd. 433 (2007) 274–278.
[7] T. Mori, T. Ikegami, H. Yamamura, J. Electrochem. Soc. 146 (1999) 4380–4385.
[8] J.R. McBride, K.C. Hass, B.D. Poindexter, W.H. Weber, J. Appl. Phys. 76 (1994) 2435–2441.
[9] C. Peng, Y. Wang, K. Jiang, B.Q. Bin, H.W. Liang, J. Feng, J. Meng, J. Alloys Compd. 349 (2003) 273–278.
[10] M.F. Luo, W.J. Shan, P.L. Ying, J.Q. Lu, C. Li, Stud. Surf. Sci. Catal. 138 (2001) 61–68.
[11] M.G. Chourashiya, J.Y. Patil, S.H. Pawar, L.D. Jadhav, Mater. Chem. Phys. 109 (2008) 39–44.

[12] R.D. Shannon, Acta Cryst. A32 (1976) 751–767.
[13] D.D. Upadhyaya, R. Bhat, S. Ramanathan, S.K. Roy, H. Schubert, G. Petzow, J. Eur. Ceram. Soc. 14 (1994) 337–341.
[14] Z.Y. Pu, J.Q. Lu, M.F. Luo, Y.L. Xie, J. Phys. Chem. C 111 (2007) 18695–18702.
[15] H. Yamamura, S. Takeda, K. Kakinuma, Solid State Ionics 178 (2007) 889–893.
[16] A.A. David, I.S. Sergei, V.S. Natalia, A.A. Igor, J. Börje, PNAS 103 (2006) 3518–3521.
[17] G.M. Christie, F.P.F. van Berkel, Solid State Ionics 83 (1996) 17–27.
[18] J.T.S. Irvine, D.C. Sinclair, A.R. West, Adv. Mater. 2 (1990) 132–138.
[19] X.J. Chen, K.A. Khor, S.H. Chan, L.G. Yu, Mater. Sci. Eng. A 374 (2004) 64–71.
[20] M. Dudek, J. Eur. Ceram. Soc. 28 (2008) 965–971.